

# MODEL AND OPTIMIZATION OF ORGANIC PHOTOVOLTAIC CELLS

By

**Amelia McNamara**

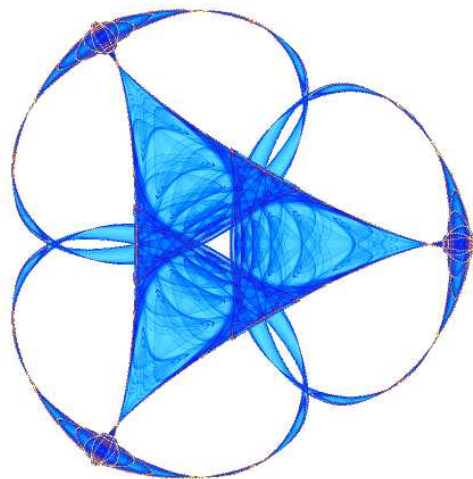
**Jordan Seering**

and

**Yi Zeng**

**IMA Preprint Series # 2271**

( August 2009 )



**INSTITUTE FOR MATHEMATICS AND ITS APPLICATIONS**

UNIVERSITY OF MINNESOTA  
400 Lind Hall  
207 Church Street S.E.  
Minneapolis, Minnesota 55455-0436

Phone: 612/624-6066 Fax: 612/626-7370

URL: <http://www.ima.umn.edu>

# Model and Optimization of Organic Photovoltaic Cells\*

Amelia McNamara,<sup>†</sup> Jordan Seering,<sup>‡</sup> and Yi Zeng<sup>§</sup>

July 30, 2009

**Abstract.** This paper focuses on optimizing the organic photovoltaic cell, an important topic in the energy industry which has not been well studied. We are especially interested in the optimization of the two active layers in the solar cell, the PEOPT polymer and the  $C_{60}$  (Fullerene) layer. Using a numerical scheme (the finite difference method) we solve the diffusion equation of excitons in the one dimensional case, and implement it with two different accepted models of energy dissipation. This allows us to compare the exciton density and flux across the heterojunction between active layers which each model produces. Using our preferred model, we optimize the layer thicknesses of the two active layers, PEOPT and  $C_{60}$  and determined them to be 12 nm and 40 nm respectively. We extend our analysis to a two-dimensional case including a curved boundary at the donor-acceptor heterojunction, using the simpler model, and study the effect of such a boundary on the conversion efficiency.

**Key words:** organic solar cell, polymer layer, electric field distribution, layer thickness, boundary shape.

## 1 Introduction and Motivation

Organic photovoltaic cells are an alternative energy source that converts light into electricity through the use of organic compounds. Although the first two-layer photovoltaic system was reported in 1958 [9], the topic did not catch much attention until a conjugated polymer was used in the cell [6]. Even though the efficiency of organic solar cells is still relatively low as compared to that of inorganic solar cells, organic systems constructed by conjugated polymers have many advantages. In contrast to the typical silicon-based solar cells, organic cells can be formed from extremely thin layers of different materials and can be easily produced. For example, whereas silicon cells must be painstakingly created out of silicon ingots, organic cells can be easily printed onto many materials— even fabric.

Much effort has been devoted to studying the mechanism of polymer solar cells, however, due to the complexity of this system, as in depth analysis of which would involve quantum mechanics, semiconductor physics, and polymer science, the mechanism is not yet completely understood. Even though several successful models have been set up for the traditional inorganic solar cells [2, 3, 4, 5, 15], the organic photovoltaic system is very different from the inorganic case. Unlike the three dimensional lattices and chemical bonds in most inorganic compounds, polymer chains always have the crystalline-amorphous structure which is weakly bonded by van der Waals forces and other weak forces including  $\pi$ - $\pi$  stacking [7]. Another main difference between the polymer and the inorganic cell is the product from the photon absorption in the cell. In most inorganic systems, free electrons and holes can be generated directly after absorbing photons [1], while in polymers, holes and electrons remain bonded pairwise as excitons at room temperature [12]. Without a doubt, this indicates that theoretical models for traditional silicon-based solar cells may not be applied to organic photovoltaic system. Instead, some new approaches modeling the diffusion of excitons rather than free charges inside the cell make good progress [7, 11, 13]. Considering the diffusion of excitons is also one of the key ideas in this work.

Moreover, an important problem scientists face is how to design the organic solar cell. As is already known, the diffusion range of excitons is about ten times shorter than the optical absorption depth [14]. To balance

---

\*This paper reports on the results obtained during the 2009 IMA Interdisciplinary REU, June 28 to July 31.

<sup>†</sup>Department of Mathematics and Computer Science, Macalester College, St. Paul, MN 55105 (amcnamar@macalster.edu).

<sup>‡</sup>School of Mathematics, University of Minnesota-Twin Cities, Minneapolis, MN 55455 (seeri002@umn.edu).

<sup>§</sup>Department of Mathematics, University of Illinois at Urbana-Champaign, Urbana, IL 61801 (yizeng2@illinois.edu).

these two factors we need to find an optimal thickness of the active layers in the solar cell. Furthermore, the shape of the boundary of each layer may also affect the efficiency of the cell, since a curved interface can increase the surface area of the heterojunction. In this paper our goal is to make some improvements on the known organic solar cell model and try to contribute to a better understanding of an optimal design of the organic solar cells.

The cells we are studying are composed of a layer of glass, a layer of ITO (Indium tin oxide), a layer of poly(3,4-ethylenedioxythiophene)-poly(styrenesulfonate) (PEDOT-PSS), a layer of poly(3-(4'-(1'',4'',7''-trioxaocetyl)-phenyl)thiophene) (PEOPT), a layer of  $C_{60}$  (Fullerene), and a layer of aluminum. A diagram of this layout is shown in Figure 1.



Figure 1: Qualitative arrangement of layers in solar cell

While we are trying to optimize the layer thicknesses for current production, we must have a baseline arrangement of layers within the cell. In many of the figures that follow, one of the layer thicknesses will be changed to view its effect on the overall system, but the rest of the layers remain the same. If not otherwise specified, the default layer thicknesses we used were those proposed by [11]:

ITO: 120 nm  
 PEDOT: 110 nm  
 PEOPT: 40 nm  
 $C_{60}$ : 35 nm  
 Al: 80 nm.

The materials that produce the most excitons, and thus the most charge carriers, are the PEOPT polymer and the fullerene ( $C_{60}$ ). These are the layers we are most interested in studying, especially the heterojunction between these two important materials. Molecular diagrams of various materials within the cell are shown in Figure 2, with the structure of PEDOT given in Figure 2(a), a diagram of PSS given in 2(b), a diagram of PEOPT in Figure 2(c), and the structure of the  $C_{60}$  Fullerene shown in Figure 2(d).

This paper is structured as follows. In Section 2 we set up a numerical scheme (using the finite difference method) for solving the diffusion equation of excitons in the one dimensional case, under two different boundary conditions. In Section 3 we compare the differences between two models of the time average of energy dissipated per second within the solar cell,  $Q_j(x)$ . The first one, proposed by [4], is a simple exponentially decaying model for the energy dissipated per second. The second uses the distribution of the electric field, a derivation for which, in the case when incident light is normal to the plane of incidence, is provided in Section 4. In Section 5 we give an analysis of the difference between exciton densities calculated with both models of  $Q_j(x)$ . In

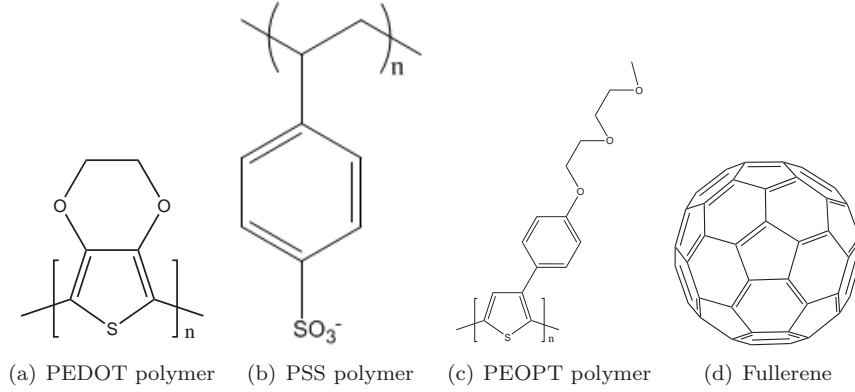


Figure 2: Molecular structures of various materials within the solar cell (a) poly(3,4-ethylenedioxythiophene) (PEDOT), (b) poly(styrenesulfonate) anion ( $\text{PSS}^-$ ), (c) poly(3-(4'-(1'',4'',7''-trioxaoctyl)-phenyl)thiophene) (PEOPT), and (d)  $\text{C}_{60}$  Fullerene

Section 6 we explain how we optimized the layer thicknesses of both PEOPT and  $\text{C}_{60}$ . Section 7 provides a comparison of the flux at the interface of the active layers described by both models of  $Q_j(x)$ . An investigation of how a curved boundary at the donor-acceptor heterojunction affects the total current density is provided in Section 8. This was done by solving boundary value problems with the aid of Comsol Multiphysics <sup>®</sup>. Finally, Section 9 is the conclusion of our study and gives some expectations for future research.

## 2 Solving the Diffusion Equation, 1D Case

In organic photovoltaic cells, photocurrent is generated by the excitons that disassociate at the donor-acceptor heterojunction. We begin our analysis by examining the system described in Figure 1 in a one-dimensional case, where light enters the cell at a  $90^\circ$  angle. In this case, we can consider the transmission and reflection of light through the cell without taking into account any light that deviates from its perpendicular path through the cell. Obviously, this is not an accurate description of what would occur in the real world, but it allows us to study the behavior of the cell in a simplified way. We model exciton diffusion within the layers of the cell by the standard diffusion equation. For each of the active layers,

$$\frac{\partial n_j}{\partial t} = D_j \frac{\partial^2 n_j}{\partial x^2} - \frac{n_j}{\tau} + \frac{\theta_1}{h\nu} Q_j(x), \quad (1)$$

where the subscripts denote the  $j$ th layer. In Equation 1,  $n_j$  is the exciton density of layer  $j$ ,  $\theta_1$  is the quantum efficiency of exciton generation,  $\tau$  is the mean lifetime of the exciton,  $h\nu$  is the excitation energy of the incident light,  $D_j$  is the diffusion constant, and  $Q_j(x)$  is the time average of energy dissipated per second. Since we are considering the case where the exciton density is time independent, i.e., the photogeneration is in equilibrium, Equation 1 can be turned into the following ordinary differential equation since  $\partial n/\partial t = 0$ .

$$\frac{d^2 n_j}{dx^2} = \beta_j^2 n_j - \frac{\theta_1}{D_j h\nu} Q_j(x), \quad (2)$$

where  $\beta_j = 1/L_j = 1/\sqrt{D_j \tau}$ , the reciprocal of the diffusion length  $L_j$ . We will approximate solutions to Equation 2 by using the Finite Difference method. Using Taylor series expansion, one can show that

$$f'(x) = \frac{f(x+h) - f(x-h)}{2h} + O(h), \quad (3)$$

$$f''(x) = \frac{f(x+h) - 2f(x) + f(x-h)}{h^2} + O(h). \quad (4)$$

We proceed in the following way: consider each layer and choose  $N$  equally spaced points where  $S = \{x_i : 1 \leq i \leq N\}$ . Consider an arbitrary point  $x_i \in S$ . The exciton density,  $n_j^{(i)} = n_j(x_i)$  at  $x_i$ , satisfies Equation 2:

$$\frac{d^2 n_j^{(i)}}{dx^2} = \beta_j^2 \cdot n_j^{(i)} - \gamma_j \cdot Q_j(x), \quad (5)$$

where  $\gamma_j = \frac{\theta_1}{D_j h \nu}$  is constant within a particular layer,

$$\frac{d^2 n_j^{(i)}}{dx^2} = \left. \frac{d^2 n^{(i)}(x)}{dx^2} \right|_{x=x_i},$$

and  $E(x_i)$  is the electric field at point  $x_i$ .

By the Finite Difference Method,

$$\frac{d^2 n_j^{(i)}}{dx^2} \approx \frac{n_j^{(i+1)} - 2n_j^{(i)} + n_j^{(i-1)})}{h^2}, \quad (6)$$

where  $h$  is the length of the step between two adjacent points. Equation 5 can be approximated by

$$\frac{1}{h^2} [n_j^{(i+1)} - 2n_j^{(i)} + n_j^{(i-1)}] = \beta_j^2 \cdot n_j^{(i)} - \gamma_j \cdot Q_j(x). \quad (7)$$

The following equation is a rearrangement of Equation 7 into a more convenient form to work with:

$$n_j^{(i+1)} - (2 + h^2 \beta_j^2) \cdot n_j^{(i)} + n_j^{(i-1)} = -\gamma_j h^2 \cdot Q_j(x), \quad (8)$$

For simplicity of notation, we drop the subscript index and restrict our attention to one of the layers. With slight abuse of notation, let us denote  $n_j^{(i)} = n_i$ . In order to solve this numerically, we must put it into matrix form,  $A \cdot \vec{n} = \vec{a}$ , where  $A$  is an  $N \times N$  matrix,  $\vec{n}$  is the vector of values of exciton density at the  $N$  mesh points we defined earlier, and  $\vec{a}$  is a column vector containing the values of  $Q_j(x)$  at the mesh points. While there are slight differences to the equation depending on the desired boundary conditions, the general form of the equation is,

$$\begin{bmatrix} -2 - h^2 \beta^2 & 1 & 0 & 0 & \dots & 0 \\ 1 & -2 - h^2 \beta^2 & 1 & 0 & \dots & 0 \\ \vdots & \ddots & \ddots & \ddots & \ddots & \vdots \\ 0 & 0 & \dots & 1 & -2 - h^2 \beta^2 & 1 \\ 0 & 0 & \dots & 0 & 1 & -2 - h^2 \beta^2 \end{bmatrix} \cdot \begin{bmatrix} n_1 \\ n_2 \\ \vdots \\ \vdots \\ n_N \end{bmatrix} = -\gamma h^2 \cdot \begin{bmatrix} a_1 \\ a_2 \\ \vdots \\ a_{N-1} \\ a_N \end{bmatrix}.$$

The entries that are changed to represent different boundary conditions are the the first two entries of the first row of  $A$ , the final two entries in the last row of  $A$ , and the first and last entry in  $\vec{a}$ . Since the excitons can disassociate easily at the interface of different layers, we could enforce Dirichlet boundary conditions; that is,  $n_1 = 0$  and  $n_N = 0$ . The Dirichlet boundary conditions require that the previous matrix be replaced with

$$\begin{bmatrix} 1 & 0 & 0 & 0 & \dots & 0 \\ 1 & -2 - h^2 \beta^2 & 1 & 0 & \dots & 0 \\ \vdots & \ddots & \ddots & \ddots & \ddots & \vdots \\ 0 & 0 & \dots & 1 & -2 - h^2 \beta^2 & 1 \\ 0 & 0 & \dots & 0 & 0 & 1 \end{bmatrix} \cdot \begin{bmatrix} n_1 \\ n_2 \\ \vdots \\ \vdots \\ n_N \end{bmatrix} = -\gamma h^2 \cdot \begin{bmatrix} 0 \\ a_2 \\ \vdots \\ a_{N-1} \\ 0 \end{bmatrix}.$$

Another choice for the boundary conditions is to only restrict the boundary between two active layers to homogeneous Dirichlet conditions, while the others are restricted to homogeneous Neumann conditions, that

is, the derivative of the exciton density with respect to  $x$  is equal to zero. In our case, for the donor layer, PEOPT, the matrix turns into

$$\begin{bmatrix} -1 & 1 & 0 & 0 & \dots & 0 \\ 1 & -2 - h^2\beta^2 & 1 & 0 & \dots & 0 \\ \vdots & \ddots & \ddots & \ddots & \ddots & \vdots \\ 0 & 0 & \dots & 1 & -2 - h^2\beta^2 & 1 \\ 0 & 0 & \dots & 0 & 0 & 1 \end{bmatrix} \cdot \begin{bmatrix} n_1 \\ n_2 \\ \vdots \\ \vdots \\ n_N \end{bmatrix} = -\gamma h^2 \cdot \begin{bmatrix} 0 \\ a_2 \\ \vdots \\ a_{N-1} \\ 0 \end{bmatrix},$$

and for the acceptor layer,  $C_{60}$ , becomes

$$\begin{bmatrix} 1 & 0 & 0 & 0 & \dots & 0 \\ 1 & -2 - h^2\beta^2 & 1 & 0 & \dots & 0 \\ \vdots & \ddots & \ddots & \ddots & \ddots & \vdots \\ 0 & 0 & \dots & 1 & -2 - h^2\beta^2 & 1 \\ 0 & 0 & \dots & 0 & -1 & 1 \end{bmatrix} \cdot \begin{bmatrix} n_1 \\ n_2 \\ \vdots \\ \vdots \\ n_N \end{bmatrix} = -\gamma h^2 \cdot \begin{bmatrix} 0 \\ a_2 \\ \vdots \\ a_{N-1} \\ 0 \end{bmatrix}.$$

### 3 Energy Dissipated per Second

While we have introduced a method for solving the differential equation, we have not yet specified the form of the exciton generation term  $Q_j(x)$ . This is a crucial part of solving the equation, and we considered two separate models.

The first model assumes that the energy dissipated per second decays exponentially, and was used in [4]. This model is given by

$$Q_j(x) = \alpha_j I_0 e^{-\alpha_j x}, \quad x \in \text{layer } j, \quad (9)$$

where  $I_0$  is the initial intensity and

$$\alpha_j = \frac{4\pi k_j}{\lambda}. \quad (10)$$

Henceforth, we will refer to this model of  $Q_j(x)$  as the simple model. This model is easy to compute, because it only depends on the initial light intensity at the heterojunction between each pair of layers and some material parameters. However, it only offers a crude approximation of  $Q_j(x)$  because it ignores reflections and interference inside the solar cell. A graph of the the energy dissipation per second over all five layers of the cell as modeled by Equation 9 can be seen in Figure 3.

A more accurate description of  $Q_j(x)$  can be modeled using the distribution of the electric field. The derivation of the electric field equations will be shown in the next section, but for now we will refer to the electric field at a point  $x$  in layer  $j$  as  $E_j(x)$ . The model that uses the electric field was proposed by [11] and is as follows:

$$Q_j(x) = \frac{1}{2} c \epsilon_0 \alpha_j \eta_j |E_j(x)|^2, \quad x \in \text{layer } j, \quad (11)$$

where  $\alpha_j$ , the absorption coefficient, is given by Equation 10. In our calculations, we often neglected the  $c$  and  $\epsilon_0$  terms, because they are constant at all points within the cell. From here forward, we will refer to this model of  $Q_j(x)$  as the sophisticated model. A graph of the energy dissipation per second over all five layers of the cell as modeled by Equation 11 can be seen in Figure 4.

While Equation 11 represents a more accurate picture of the behavior of the excitons, it is computationally expensive as compared to Equation 9 and does not generalize easily to the situation where the heterojunction between layers is not a flat boundary. Because of this, we will be using Equation 9 when we move on to studying the effect of curved boundaries between layers.

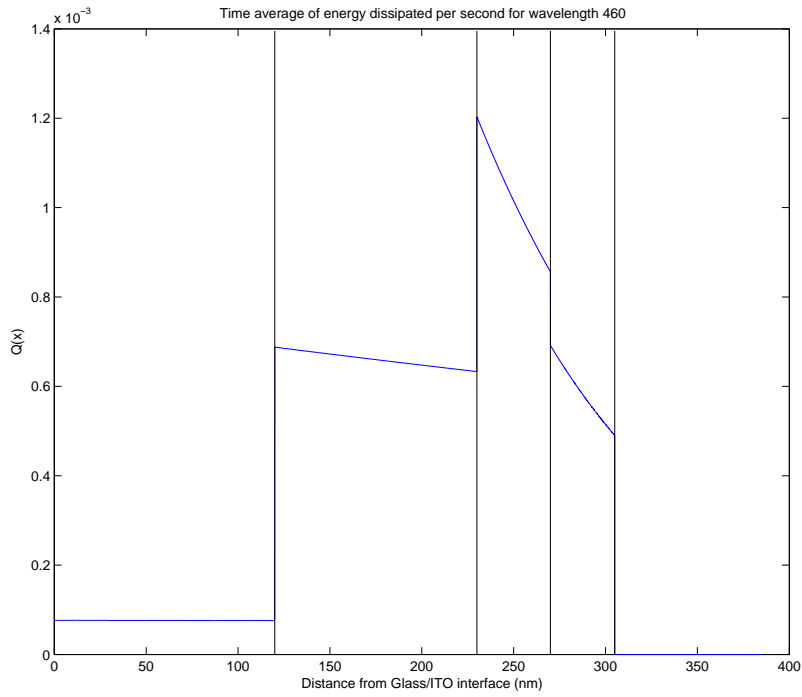


Figure 3: Energy dissipated per second, as modeled by Equation 9 (simple exponential model)

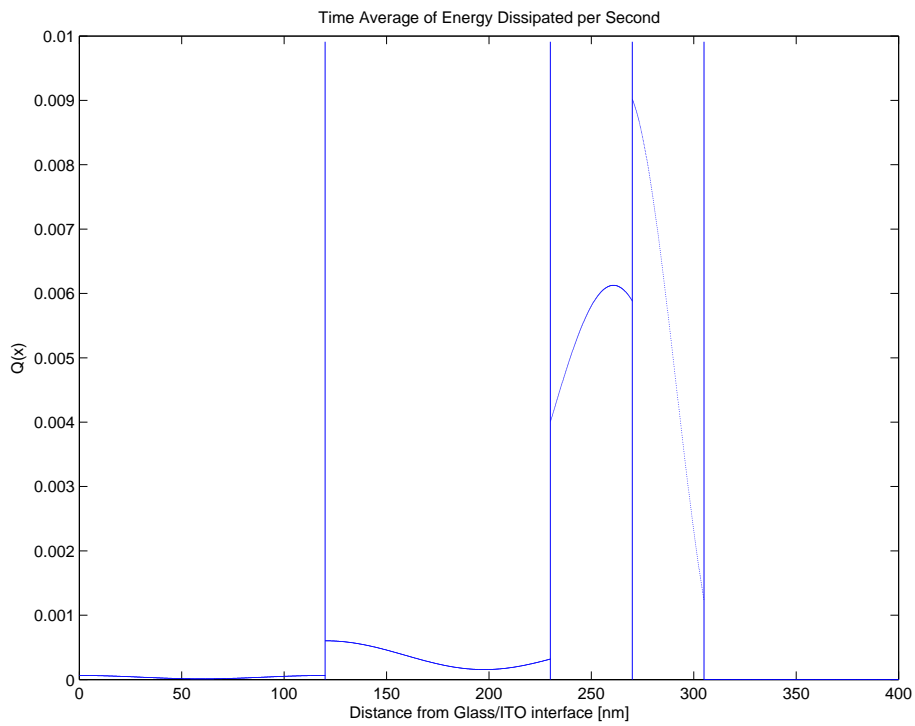


Figure 4: Energy dissipated per second, as modeled by Equation 11 (sophisticated model of  $Q(x)$ )

## 4 Electric Field Distribution

A solar cell converts photon energy into electric energy by absorbing light. Light is an electromagnetic wave and one property of light is that it produces an electric field, a concept introduced by Michael Faraday. An electric field can be created under the presence of a time-varying magnetic field. First, we must consider the electric field distribution of light at every point inside the solar cell. According to Maxwell's equations from the laws of electricity and magnetism, in the time harmonic case or time-invariant system (as represented in [8]) are,

$$\nabla \times \vec{E} = -i\omega\mu\vec{H}, \quad (12)$$

$$\nabla \times \vec{H} = \vec{J} + i\omega\epsilon\vec{E}, \quad (13)$$

where  $\epsilon$  is the electric permittivity,  $\mu$  is the magnetic permeability,  $\omega$  is the angular frequency,  $\vec{E}$  is the electric field, and  $\vec{H}$  is the magnetic field. Note that  $\omega = 2\pi f$ , where  $f$  is the sinusoidal frequency. Moreover, the total current,  $\vec{J} = \vec{J}_s + \sigma\vec{E}$ , such that  $\vec{J}_s = 0$  in free space where  $\vec{J}_s$  is the source current and  $\sigma$  is the electrical conductivity of the material. For air,  $\sigma$  ranges from  $0.3 \times 10^{-14}$  S/m to  $0.8 \times 10^{-14}$  S/m, ergo we set  $\vec{J} = 0$ . Before the light enters the solar cell, there is no source current.

While incident light can strike the surface of the solar cell at any angle  $\Theta \in [0, \pi/2]$ , we considered the simplest case for light with the electric field perpendicular to the plane of incidence. Therefore the electric field  $\vec{E}$  and the magnetic field  $\vec{H}$  are of the form

$$\vec{E}(x) = (0, E_y(x), 0), \quad (14)$$

$$\vec{H}(x) = (0, 0, H_z(x)), \quad (15)$$

such that only the  $y$  component  $E_y(x)$  of the electric field is nonzero and only the  $z$  component  $H_z(x)$  of the magnetic field is nonzero. Plugging the two vectors from Equations 14 and 15 into Equations 12 and 13 produces the following

$$\frac{\partial E_y}{\partial x} = i\omega\mu H_z, \quad (16)$$

$$\frac{\partial H_z}{\partial x} = i\omega\epsilon E_y. \quad (17)$$

Differentiating Equation 16 with respect to  $x$  turns it into a second-order equation

$$\frac{\partial^2 E_y}{\partial x^2} = i\omega\mu \frac{\partial H_z}{\partial x}. \quad (18)$$

Furthermore, substituting Equation 17 for  $\frac{\partial H_z}{\partial x}$  into Equation 18 produces

$$\frac{\partial^2 E_y}{\partial x^2} = -\omega^2\epsilon\mu E_y, \quad (19)$$

or, written in a simpler form

$$E_y''(x) + \omega^2\epsilon\mu E_y(x) = 0, \quad (20)$$

where  $'$  denotes differentiating with respect to  $x$ . The general solution to Equation 20 is

$$E_y(x) = \tilde{A} \cos(\omega\sqrt{\epsilon\mu} \cdot x) + \tilde{B} \sin(\omega\sqrt{\epsilon\mu} \cdot x) = Ae^{i\omega\sqrt{\epsilon\mu} \cdot x} + Be^{-i\omega\sqrt{\epsilon\mu} \cdot x}, \quad (21)$$

where A and B are constants that can be uniquely determined given specific boundary conditions. In a similar manner, we can find the equation for the magnetic field

$$H_z(x) = \sqrt{\frac{\epsilon}{\mu}} [\tilde{A} \cos(\omega\sqrt{\epsilon\mu} \cdot x) - \tilde{B} \sin(\omega\sqrt{\epsilon\mu} \cdot x)] = \sqrt{\frac{\epsilon}{\mu}} [Ae^{i\omega\sqrt{\epsilon\mu} \cdot x} - Be^{-i\omega\sqrt{\epsilon\mu} \cdot x}]. \quad (22)$$

We followed the derivation from [16] for the particular case when  $\Theta = 90^\circ$  case. We begin by defining

$$z_j = \sqrt{\frac{\mu_j}{\epsilon_j}}, \quad (23)$$



where subscripts denote the layers and  $z_j$  is the impedance which has the unit of ohm ( $\Omega$ ) in the  $j$ th layer. From here on, we will drop the subscript  $y$  from  $E_y$  and the subscript  $z$  from  $H_z$ .

We use a coordinate system in the solar cell, as described in Figure 5. Light will enter the cell at the “top” and, through many reflections and transmissions, reach the “bottom” of the cell ( $x = 0$ ).  $|E_0|^2$  is the initial intensity of the electric field. The arrows represent the light being absorbed and reflected. We assumed that the area above and below the cell is air and semi-infinte. No light is entering through the bottom of the cell at  $x = 0$ .

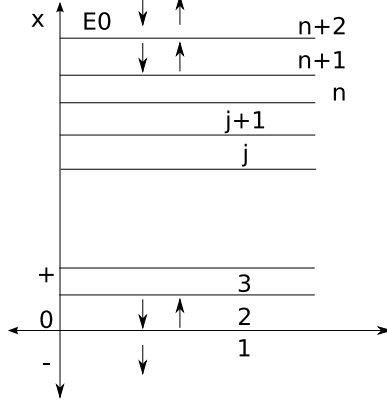


Figure 5: Layers of solar cell used for derivation of electric field

We begin with layer 2 (in our case the Aluminum layer). Because the heterojunction between layer 1 and layer 2 is at  $x = 0$ , the exponential term simplifies to 1 and our general solution becomes

$$E(0) = A_2 e^{i\omega_2 \sqrt{\epsilon_2 \mu_2} \cdot 0} + B_2 e^{-i\omega_2 \sqrt{\epsilon_2 \mu_2} \cdot 0} = A_2 + B_2.$$

Similarly, from Equation 22

$$H(0) = \frac{A_2 - B_2}{z_2}.$$

Still considering the special case at the “bottom” layer (where no light is reflected) we define new variables  $z_{in}^{(j)}$ ,  $j = 1, \dots, n+1$ . The variable  $z_{in}^{(j)}$  signifies the ratio between the electric field and the magnetic field at the entrance of the  $j$ th layer.

$$z_{in}^{(1)} = \frac{E(0)}{H(0)} = \frac{A_2 + B_2}{A_2 - B_2} z_2. \quad (24)$$

Consider layer 1 (air) at  $x = 0$ . The assumption that no light is being reflected from the bottom requires  $B_1 = 0$  which implies  $E(0)/H(0) = z_1$ . According to electromagnetic theory,  $E$  and  $H$  must be continuous at the interface, therefore

$$z_{in}^{(1)} = \frac{E(0)}{H(0)} = z_1. \quad (25)$$

Now that we have seen its application in a specific case, we can move on to the general case. We will examine the heterojunction between  $j$  and  $j+1$ .

$$z_{in}^{(j)} = \frac{A_{j+1} + B_{j+1}}{A_{j+1} - B_{j+1}} \cdot z_{j+1} = \frac{A_j e^{i\phi_j} + B_j e^{-i\phi_j}}{A_j e^{i\phi_j} - B_j e^{-i\phi_j}} \cdot z_j, \quad (26)$$

where  $\phi_j = \omega_j \sqrt{\epsilon_j \mu_j} d_j$ , while  $d_j$  is the thickness of the  $j$ th layer.

By substituting  $j$  for  $j-1$  into Equation 26 we get

$$z_{in}^{(j-1)} = \frac{A_j + B_j}{A_j - B_j} \cdot z_j. \quad (27)$$

We can perform an algebraic manipulation to show that

$$z_{in}^{(j)} = \frac{z_{in}^{(j-1)} + iz_j \tan \phi_j}{z_j + iz_{in}^{(j-1)} \tan \phi_j}. \quad (28)$$

We already know that  $z_{in}^{(1)} = z_1$ , thus we can solve  $z_{in}^{(j)}$  for every  $j$  by induction.

Again, considering Equation 26 and the continuity of E and H at the interface of the  $j$ th and the  $(j + 1)$ st layers

$$E = A_j e^{i\phi_j} + B_j e^{-i\phi_j} = A_{j+1} + B_{j+1}, \quad (29)$$

$$H = \frac{A_j e^{i\phi_j} + B_j e^{-i\phi_j}}{z_j} = \frac{A_{j+1} - B_{j+1}}{z_{j+1}}. \quad (30)$$

Solving Equations 26, 29, and 30 we derive a relation between the  $A$  coefficients for adjacent layers

$$\frac{A_j}{A_{j+1}} = \frac{z_j + z_{in}^{(j)}}{z_{j+1} + z_{in}^{(j)}} e^{-i\phi_j}. \quad (31)$$

For a  $k$ -layer solar cell  $A_{k+2}$  is the incidence of light which is known, therefore every  $A_{2 \leq j \leq k+1}$  can be determined.

Since  $A$  is known for every layer, it is easy to obtain  $B$  for every layer by using Equation 26. Once the coefficients at each heterojunction are determined, we can compute the electric field at any point within the solar cell. We have a program which takes values of  $x$  as input, determines which layer  $x$  belongs to, and uses this information to find the electric field  $E_p$  of the point  $x$  with the following formula

$$E_p = A_j e^{\omega \sqrt{\epsilon} \mu d'} + B_j e^{-\omega \sqrt{\epsilon} \mu d'}, \quad (32)$$

where  $d'$  is the distance from the bottom of the  $j$ th layer in which the point lies.

We compared our results to those found in [11]. The first result we reproduced was the distribution of the electric field within the layers of the cell at various thickness of  $C_{60}$ . These results are shown in Figures 6 and 7. These results are almost precisely the results achieved by [11], although our scale is slightly different. We considered this a success of our method.

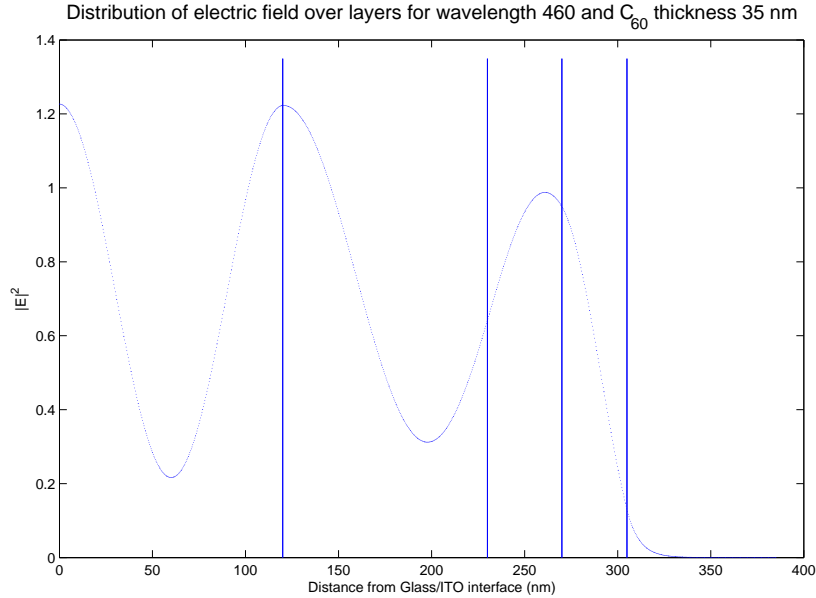


Figure 6: Distribution of electric field for  $C_{60}$  thickness of 35 nm

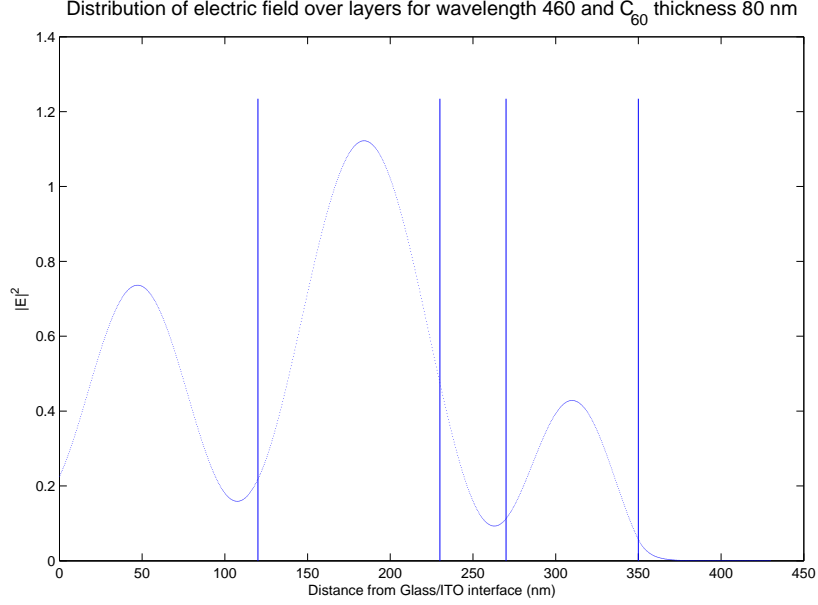
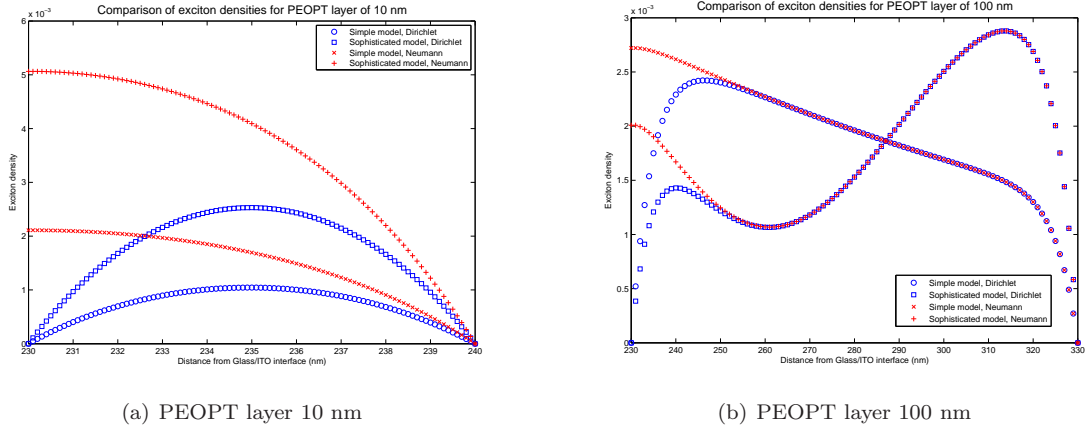


Figure 7: Distribution of electric field for  $C_{60}$  thickness of 80 nm

## 5 Model Comparison

Using both the “sophisticated model” (Equation 11) and the “simple” model (Equation 9) we solved the differential equation to determine the exciton density in the layers of interest. In order to test the qualitative behavior of the two models, we studied the behavior of the models for “thin” layers and “thick” layers. We chose 10 nm thickness for the “thin” layers and 100 nm for the “thick” layers.

For example, if the polymer is listed as 10 nm, the PEOPT layer is 10 nm and the rest of the layers maintain their default thicknesses, as given in Section 1. With these conditions, the simple model predicted exciton density profiles similar to those predicted by the sophisticated model, although the actual values are generally different. These exciton density profiles are shown in Figure 8 and Figure 9.



(a) PEOPT layer 10 nm

(b) PEOPT layer 100 nm

Figure 8: Exciton densities in polymer layer for wavelength 460. ITO (120 nm)/PEDOT (110 nm)/PEOPT/ $C_{60}$  (35 nm)/Al. In (a) the PEOPT layer is 10 nm and in (b) it is 100 nm. The simple method is described by Equation 9, the sophisticated model is described by Equation 11.

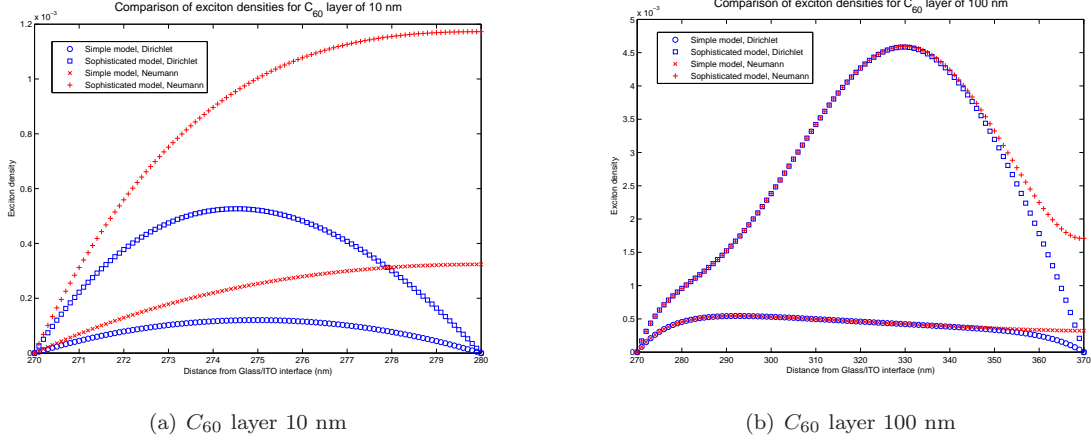


Figure 9: Exciton densities in  $C_{60}$  layer for wavelength 460. ITO (120 nm)/PEDOT (110 nm)/PEOPT (40 nm)/ $C_{60}$ /Al. In (a) the  $C_{60}$  layer is 10 nm and in (b) it is 100 nm. The simple method is described by Equation 9, the sophisticated model is described by Equation 11.

To compare the two models, we solved Equation 9 and Equation 11 using the initial intensity as one. This resulted in similarly shaped graphs from both models, but different scales. The exponential method is under-predicting the sophisticated method, by about one half. This is the result we expected, because our simple model is not taking any reflections into account. This means we lose about half of the light that is captured in our more sophisticated model. For thin layers, both the Dirichlet and Neumann boundary conditions are qualitatively matched by the two models.

The differentiation between models occurs at greater layer thicknesses. In Figure 8(b), observe that boundary conditions cease to make a difference in predicted density after the first few nm. The sophisticated model predicts the line denoted by  $\square$  for Dirichlet conditions, and the line denoted by  $+$  for Neumann boundary conditions. Notice that these two lines fall almost on top of one another after the first 20 nm. This means the sophisticated model is predicting the same exciton density within the layer, regardless of boundary conditions. The same behavior can be observed in the simple model. For this model, the Dirichlet case is denoted by  $\circ$  and the Neumann case is denoted by  $\times$ . Again, after the first 20 nm these two cases overlap, which means that regardless of boundary conditions the simple model predicts the same exciton density. However, the sophisticated and simple models are predicting very differently shaped exciton density profiles. We would hope for qualitatively similar plots, such as the one produced with the thin polymer layer, but for thick layers the models predict qualitatively different shapes.

The same basic behavior can be seen in Figure 9(b); once again the boundary condition ceases to make a difference after a few nanometers, and the shapes of the curves created by the two models are profoundly different. This shows us what a difference it makes to consider reflections within the model.

These images were created for the wavelength 460, which was the wavelength under investigation by [11] and also falls near the higher end of the visible spectrum. More analysis about the difference between the two models over the entire visible spectrum is given in Section 7.

## 6 Optimization of Active Layers

There are several different optimization methods we considered implementing regarding the thicknesses of active layers inside a photovoltaic device. One of the methods seeks to maximize the electric field at the interface of active layers because the quantity of excitons generated depends on  $|E(x)|^2$  as a result of light absorption. Figure 10 shows the magnitude of the electric field at the PEOPT/ $C_{60}$  interface and gives an optimal layer thickness of 31 nm for  $C_{60}$ . This result agrees with [11]. However, if we further decrease the thickness of PEOPT, then  $|E(x)|^2$  will continue to increase and the optimal thickness of PEOPT will approach 0 nm which contradicts physical intuition.

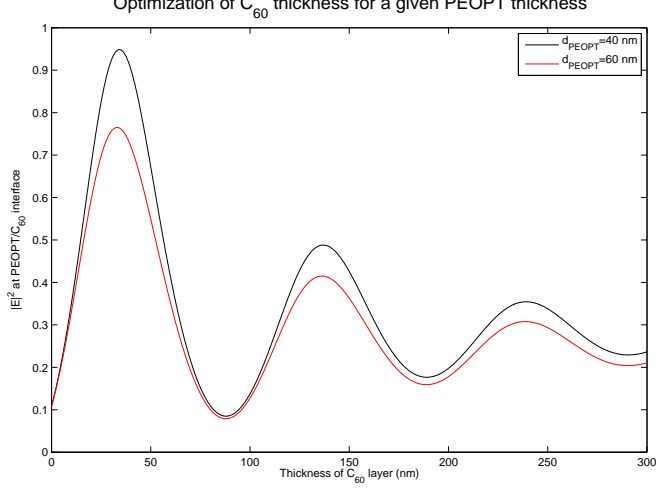


Figure 10: Optimal  $C_{60}$  thickness for PEOPT thicknesses of 40 and 60 nm, respectively

In fact, maximizing  $|E(x)|^2$  will not actually maximize the performance of the solar cell, since the diffusion of excitons is neglected when only considering the magnitude of the electric field. A more reasonable quantity to optimize is the current density for certain sunlight intensities. The current generated due to excitons produced in layer 1 can be found as

$$J_1(\lambda) = -q\theta_2 D_1 \left. \frac{\partial n_1(x, \lambda)}{\partial x} \right|_{x=d_j}, \quad (33)$$

where  $q$  is the electron charge,  $\theta_2$  is the exciton dissociation efficiency at the interface of one layer, and  $d_j$  is the thickness of the donor layer. Similarly, we can calculate the current density of the acceptor layer:

$$J_2(\lambda) = q\theta_2 D_2 \left. \frac{\partial n_2(x, \lambda)}{\partial x} \right|_{x=0}. \quad (34)$$

We assume that charge carriers are only generated at the interface of the active layers. Since charge carriers produced due to excitons generated in both layers will contribute to the current, the total current density is represented by the sum of Equations 33 and 34

$$J_{Photo}(\lambda) = q \left( -D_1 \left. \frac{\partial n_1(x, \lambda)}{\partial x} \right|_{x=d_j} + D_2 \left. \frac{\partial n_2(x, \lambda)}{\partial x} \right|_{x=0} \right), \quad (35)$$

with the assumption that  $\theta_2 = 1$ .

The incident monochromatic photon to current collection efficiency (IPCE), which is a percentage, as given in [11] is

$$IPCE(\lambda) = 1240 \cdot \frac{J_{Photo}(\lambda)}{\lambda I_0}, \quad (36)$$

where  $I_0$  is the initial intensity. If we consider the spectral distribution of the sunlight  $I(\lambda)$  (refer to [10]), we can calculate the total current of the solar cell using the following equation

$$J_{Total} = \int IPCE(\lambda) \cdot I(\lambda) \cdot d\lambda. \quad (37)$$

We fixed the thickness of ITO, PEDOT, and Aluminum, to 120 nm, 110 nm, and 100 nm respectively. Then, we varied both of the thickness of PEOPT and  $C_{60}$  from 10-140 nm. We arrived at the following result shown in Figure 11. The optimal thicknesses of PEOPT and  $C_{60}$  are approximately 10nm and 40nm respectively.

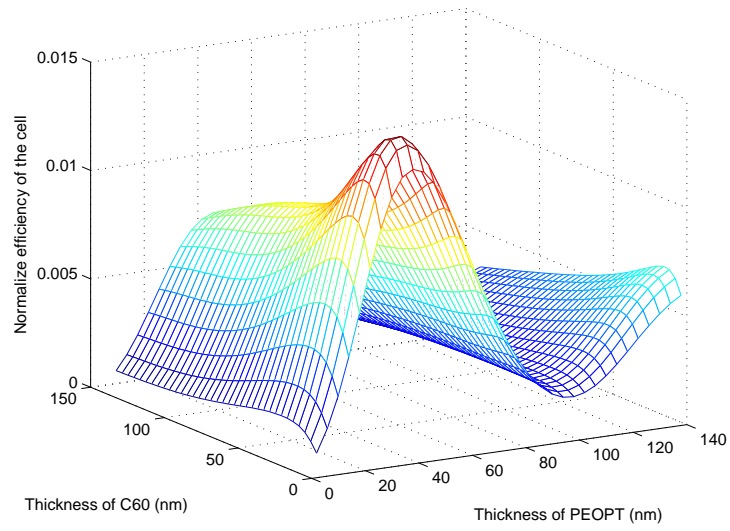


Figure 11: Global Optimization of PEOPT and C<sub>60</sub> Layer Thicknesses

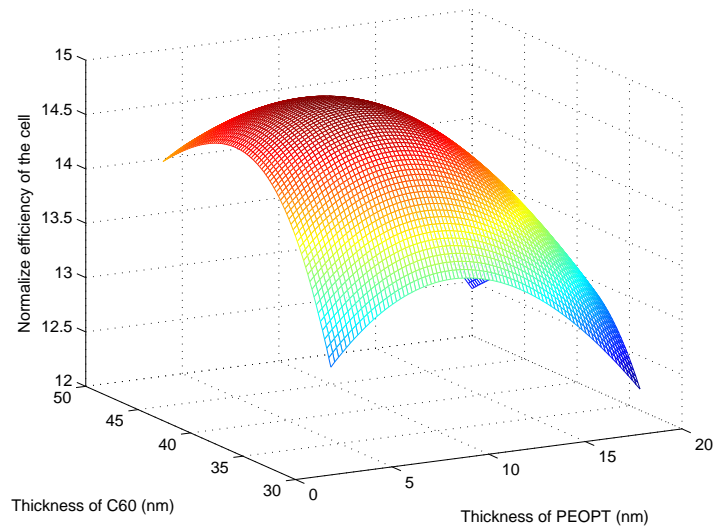


Figure 12: Local Optimization of PEOPT and C<sub>60</sub> Layer Thicknesses

Then again, varying the thickness of PEOPT from 5-20 nm and the thickness of  $C_{60}$  from 35-50 nm we produced a more accurate simulation of the local maximum shown in Figure 12.

The simulations suggest that the optimal thickness for PEOPT is 12 nm, and that the optimal thickness for  $C_{60}$  is 40 nm.

## 7 Flux Comparison

Further, we would like to study the flux in cells with non-flat boundaries between layers and how the increase in curvature and surface area of these boundaries affects the charge carrier generation. Although the “sophisticated” model is more accurate than the “simple” model, due to the complexity of carrying out a derivation analogous to the one given in Section 4 for the case of uncurved boundaries, we will need to use the “simple” model to expand our investigation. For this reason, we examine herein the difference in predicted values of flux between the two models. Flux was computed using each model, following Equation 35. Plots of the flux across the PEOPT/ $C_{60}$  layer over the visual spectrum are shown in Figure 13 and Figure 14. Once again, we have shown a “thin” and a “thick” layer (10 and 100 nm, respectively).

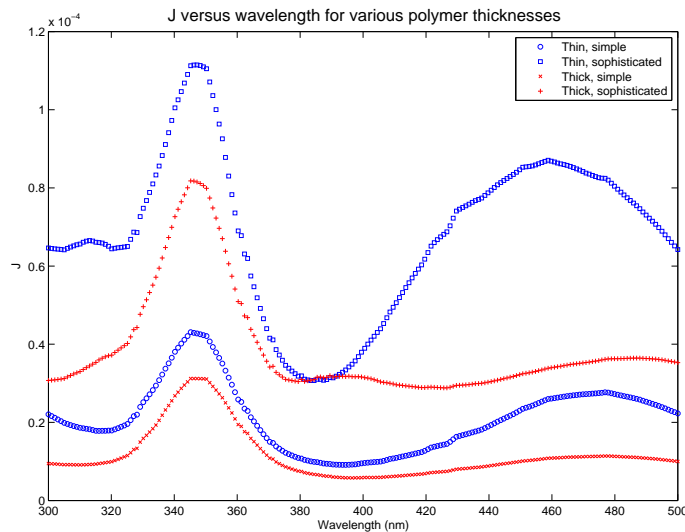


Figure 13: Flux across the PEOPT/ $C_{60}$  boundary for wavelengths from 300 to 500 nm. “Thin” is 10 nm and “thick” is 100 nm.

It is hard to determine how different the values are just by looking at the plots, so we developed a comparison system. Using the equation

$$\text{Error}(\lambda) = \frac{J_E(\lambda) - J_e(\lambda)}{J_E(\lambda)} \cdot 100, \quad (38)$$

where  $J_e(\lambda)$  is the flux given by the “simple” model and  $J_E(\lambda)$  is the flux given by the “sophisticated” model. The idea was to get a percent error that was scaled by the size of the values. Plots of these errors against wavelength can be seen in 15 and 16.

Overall, the error is not that extreme. Most of the percent errors are around 70%. For the PEOPT layer, wavelengths over 360 have the lowest errors. For the  $C_{60}$  layer, the error and the wavelength are not clearly correlated. Most of the errors in this layer are also fairly small, around 50%. The 100 nm layer had the most error, but the layers with smaller thicknesses all stayed within reasonable error ranges. As one could see in the specific plots in Figure 13 and Figure 14, the two models create graphs that are qualitatively similar, if not on the same scale with their values. This is comforting, and allows us to use the “simple” model given by Equation 9 in the next stage of our analysis: studying qualitatively how the increase of surface area of the heterojunction affects the generation of charge carriers.

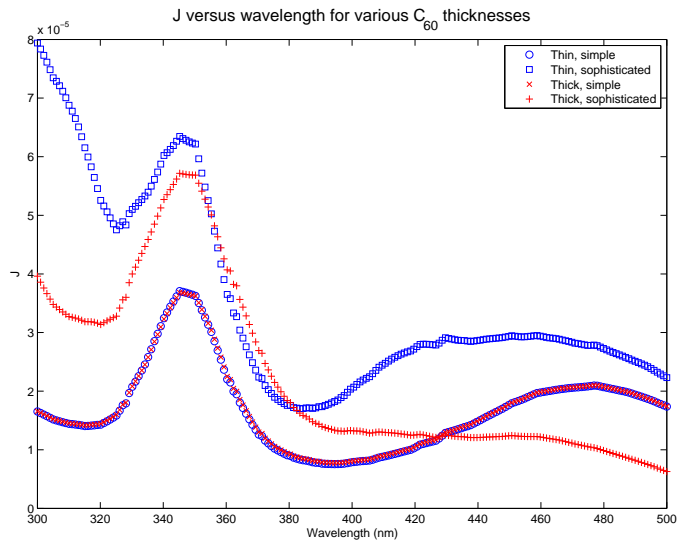


Figure 14: Flux across the PEOPT/ $C_{60}$  boundary for wavelengths from 300 to 500 nm. “Thin” is 10 nm and “thick” is 100 nm.

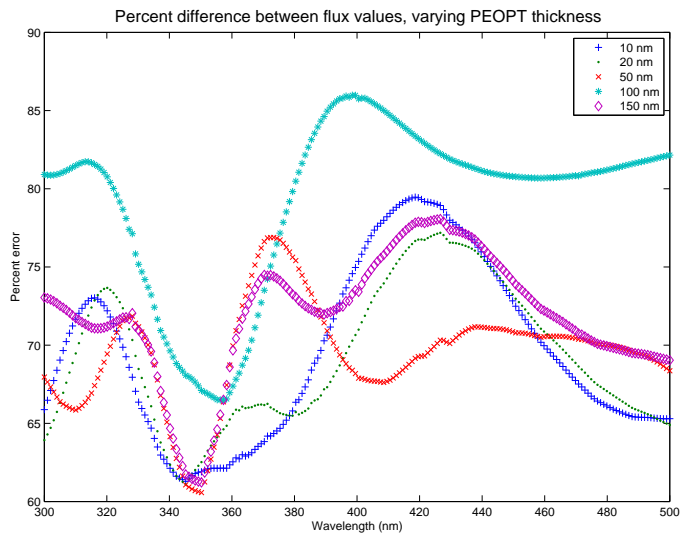


Figure 15: Average percent difference between simple exponential model and “sophisticated” model. These values are for a polymer layer of 10, 20, 50, 100 or 150 nm over the visible spectrum (300 nm - 500 nm).



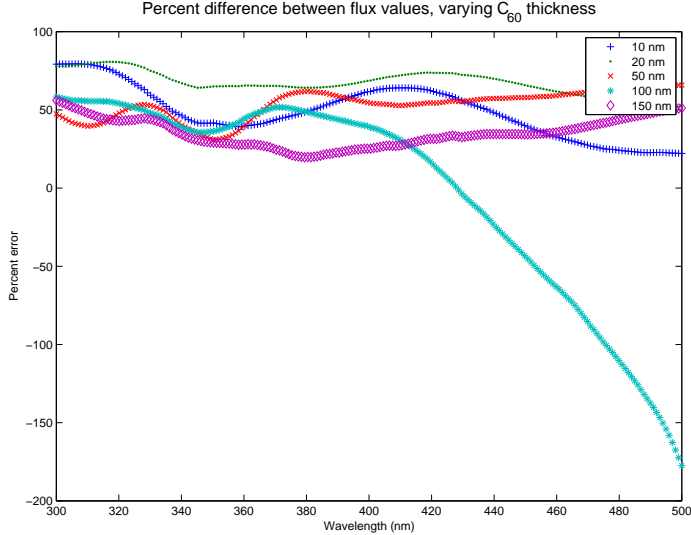


Figure 16: Average percent difference between simple exponential model and “sophisticated” model. These values are for a  $C_{60}$  layer of 10, 20, 50, 100 or 150 nm over the visible spectrum (300 nm - 500 nm).

## 8 Solving the Diffusion Equation, 2D Case

So far, our analysis has focused on the 1D-case, where the heterojunction between layers is simply a point. In order to study the effect of curved heterojunctions, we needed to expand our analysis to a 2D-case, so the heterojunction could be represented as a line. To facilitate this analysis, we used Comsol Multiphysics <sup>®</sup>.

The general form of the partial differential equation we used<sup>1</sup> is represented by Comsol in the following form:

$$e_a \frac{\partial^2 u}{\partial t^2} + d_a \frac{\partial u}{\partial t} - \nabla \cdot (c \nabla u + \alpha u - \gamma) + \beta \nabla u + au = f. \quad (39)$$

For our purposes,  $e_a = 0$ ,  $d_a = 0$ ,  $c = 1$ ,  $\alpha = 0$ ,  $\gamma = 0$ ,  $\beta = 0$ ,  $a = 1/D$ , and  $f = \frac{1}{D} \alpha I_0 e^{-\alpha x}$ .

This equation was solved over an area which was predefined within the Comsol environment. The model cell we used consisted only of the two active layers. These layers were both set at a default thickness of 2.5 with a width of 3, as is shown in Figure 17(a). The boundaries at  $y = 0$  and  $y = 3$  (the sides of our cell) were set as periodic Dirichlet boundaries. This was to avoid the width of the cell affecting the results we produced; because the edges of the cell were set as periodic, the cell was semi-infinite. The heterojunction between the two layers was also given Dirichlet conditions. The “top” and “bottom” of the cell (at  $x = 0$  and  $x = 5$ ) were either given Dirichlet or Neumann boundary conditions. We created nine distinct cell layouts, and ran each layout under both Dirichlet and Neumann boundary conditions at the “top” and “bottom” of the cell. In order to test the effect of varying the number of “waves” and the amplitude of these “waves”, we changed the boundary between the two layers to a wave centered at the middle of the cell, as shown in Figure 17(b). Our hypothesis was that an increase in surface area of the boundary would result in an increase of the amount of exciton dissociation into free charges, hence an increase in current density. To test our hypothesis, we varied the two different parameters: the number of curves in the boundary and the amplitude of the curves.

Using this Comsol environment, we solved the differential equation (using the simple exponential model) for cells with a variety of boundary shapes. Figures 17 and 18 represent the exciton density over the whole area of the active layers. These figures can be compared to the Figures 8 and 9 – their analogues in the one dimensional case.

Our first set of figures holds the amplitude of the waves at  $A = 0.5$  and varies the number of waves. The difference in the exciton distribution can be easily seen in Figure 18.

<sup>1</sup>accessed from Comsol by: Model Navigator → PDE Modes → PDE, Coefficient Form → Stationary analysis

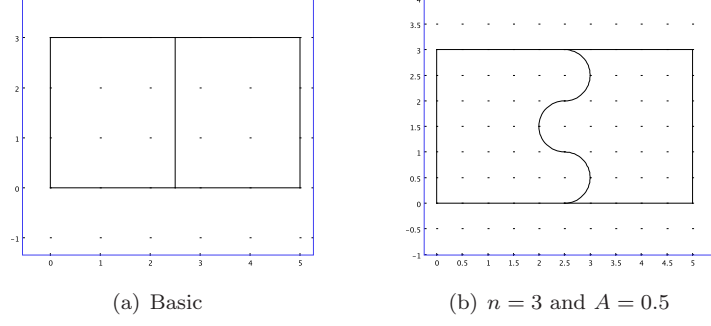


Figure 17: Setup of Consol environment

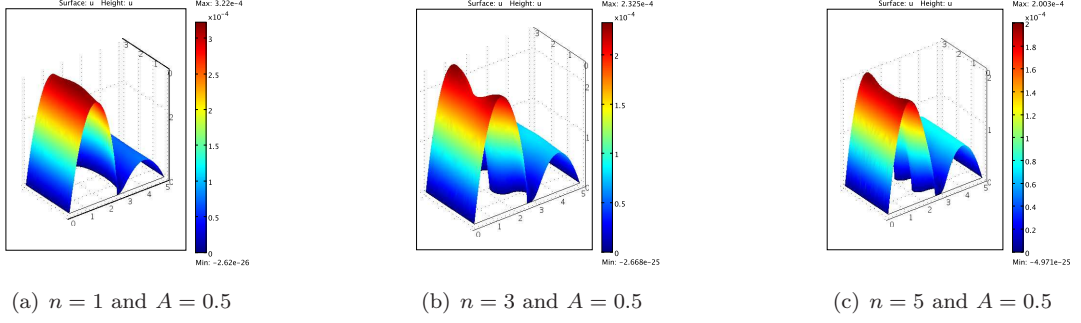


Figure 18: Exciton densities of active layers under Dirichlet boundary conditions for  $\lambda = 460$  using the simple model, varying the number of “waves”

Similarly, our second set of figures holds the number of waves at  $n = 3$  and varies the amplitude of those waves. Again, the difference in exciton densities is obvious in Figure 19. Note that the image in the center of both Figure 18 and of Figure 19 is the same. This is to facilitate reference. Analogous results were obtained when using homogeneous Neumann boundary conditions at  $x = 0$  and  $x = 5$ .

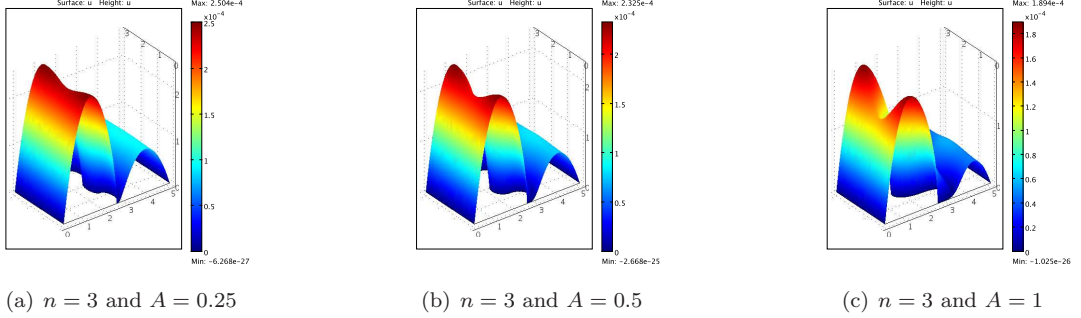
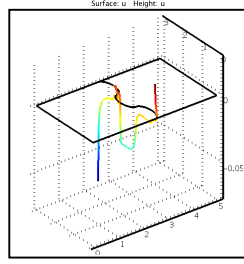


Figure 19: Exciton densities of active layers under Dirichlet boundary conditions for  $\lambda = 460$  using the simple model, varying the amplitude of the deformations (waves)

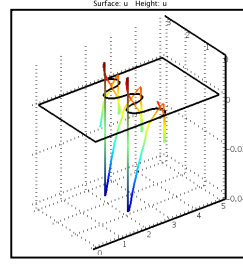
We must analyze the flux through the boundary from both  $C_{60}$  side and the PEOPT side, which allows us to calculate the total flux (as in Equation 35)

$$J_{Photo}(\lambda) = q \left( -D_1 \left. \frac{\partial n_1(x, \lambda)}{\partial x} \right|_{x=d_j} + D_2 \left. \frac{\partial n_2(x, \lambda)}{\partial x} \right|_{x=0} \right). \quad (40)$$

Figure 20 represents example plots of  $J_{Photo}$  over the entire boundary for a few of the cases we were studying.



(a)  $n = 3$  and  $A = 0.25$  Flux

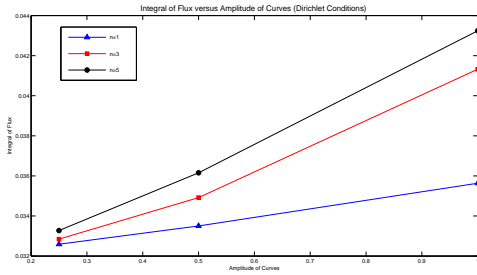


(b)  $n = 5$  and  $A = 0.5$  Flux

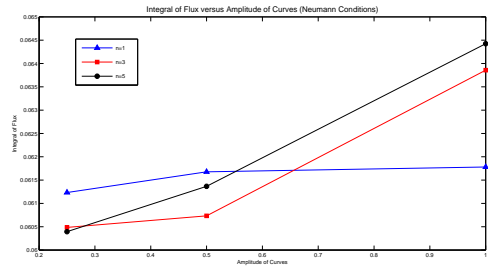
Figure 20: Flux over 2D boundaries of different shapes

To calibrate our results, we solved the differential equation using flat boundaries such as those seen in Figure 17(a) and compared the average flux obtained from the Comsol program to the value of the flux given by our 1D Matlab model. We compared two different flat-boundary models: one where the layer thicknesses were both the same (as in Figure 17(a)) and one where the first layer remained the same thickness and the second layer was increased to three times its original size. An analogous model was created in Matlab.

Figure 21 displays the total flux across the boundary for both Dirichlet and Neumann boundary conditions. Then, we found the flux per unit length by dividing the total flux by the arc length of the boundaries. These results can be seen in Figure 22. In Figures 21 and 22 the blue line represents a boundary made up of a half-ellipse, the red line represents a boundary made up of three half-ellipses, and the black line represents a boundary made up of five half-ellipses.

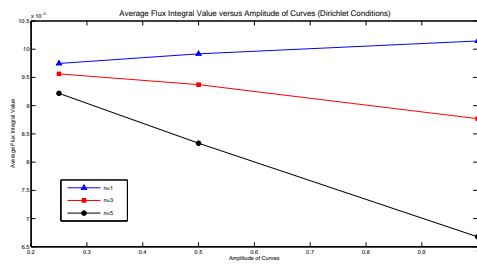


(a) Total Flux (Dirichlet Conditions)

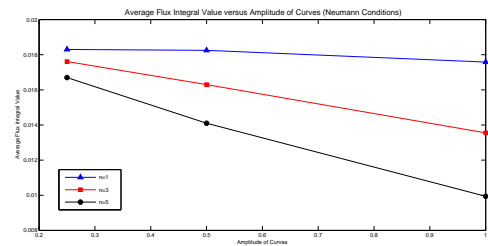


(b) Total Flux (Neumann Conditions)

Figure 21: Total Flux Across Boundaries



(a) Flux per unit length (Dirichlet Conditions)



(b) Flux per unit length (Neumann Conditions)

Figure 22: Flux per unit length Across Boundaries

From this analysis, we determined that there was a relationship between surface area and the integral of the flux. Overall, increasing the number of waves and the amplitude of the waves increased the total flux,

whereas the average flux decreased for every case except for when the boundary was made of a half-ellipse with imposed Dirichlet conditions. Therefore, a curved boundary could create a more efficient solar cell. Of course, because we employed the exponential decay model for  $f$  in Equation 39, we are limited to interpreting the behavior of the exciton density qualitatively.

## 9 Conclusion and Future Work

In this paper we optimized the thickness of the two active layers (PEOPT and  $C_{60}$ ) in organic photovoltaic solar cells, and made suggestions toward the efficacy of using curved heterojunctions between layers. This was done by solving the diffusion equation numerically, using the finite difference method, for the exciton density within the cell. An important component in the studied diffusion equation is the time average of energy dissipated per second, and we studied two models of this dissipation. Using the results from solving the diffusion equation with our preferred model of energy dissipation, we were able to find the current density at the heterojunction between the active layers (refer to Equations 35 and 40). Based on this, we optimized the layer thicknesses of PEOPT and  $C_{60}$  using Matlab. Optimal layer thicknesses of PEOPT (12 nm) and  $C_{60}$  (40 nm) were obtained by varying a reasonable range of thickness of the two active layers. In order to study the effect of a curved boundary between the active layers, we had to use the simpler model of energy dissipation, due to the difficulty generalizing the derivation of the optical electric field distribution, given in Section 4, to the case of curved boundaries. Comparisons were made between the two models to ensure that the error was not significant before we moved on to modeling the curved boundary. With the aid of Comsol Multiphysics, we were able to perform some qualitative comparisons of the current density between cells with different curvatures of the heterojunction. We determined that an increase in surface area of the boundary will result in an increase in net flux which implies an increase in short circuit current.

In order to advance this research, future effort could be devoted to the following issues. First, a more general model of the electric field distribution, which accounts for varying angles of the incident light would more realistically capture the effect of sunlight incident with the solar cell. Second, deriving a new method to calculate the accurate electric field distribution in layers with curved boundaries (to be used instead of the exponential model for the energy dissipated per second we are currently using) could help give a better guidance for the cell design. Ultimately, it is important to test the model against experimental data. We believe that these suggested improvements will allow us to better fit lab data.

## Acknowledgments

This paper reports on the results obtained during the 2009 Institute for Mathematics and its Applications (IMA) Interdisciplinary Research Experience for Undergraduates, June 28 to July 31. The authors gratefully acknowledge the IMA for providing this opportunity. As well, we sincerely thank our advisor Dr. Fadil Santosa and mentor Dr. Tsvetanka Sendova for their guidance while conducting this research. We would also like thank Dr. Russell J. Holmes and Richa Pandey for all their help and for providing the optical data we used throughout our analysis.

## References

- [1] R. H. Bube. *Photoelectronic Properties of Semiconductors*. Cambridge University Press, 1992.
- [2] A. Désormeaux, J. J. Max, and R. M. Leblanc. Photovoltaic and Electrical Properties of Al/Langmuir-Blodgett films/Ag Sandwich Cells Incorporating Either Chlorophyll a, Chlorophyll b, or Zinc Porphyrin Derivative. *Journal of Physical Chemistry*, 97:6670, 1993.
- [3] H. B. DeVore. Spectral Distribution of Photoconductivity. *Physical Review*, 102:86, 1956.
- [4] A. K. Ghosh and T. Feng. Merocyanine organic solar cells. *Journal of Applied Physics*, 49:5982, 1978.
- [5] A. K. Ghosh, D. L. Morel, T. Feng, R. F. Shaw, and C. A. Rowe Jr. Photovoltaic and Rectification Properties of Al/Mg Phthalocyanine/Ag Schottky-barrier Cells. *Journal of Applied Physics*, 44:230, 1974.
- [6] J. J. M. Halls, C. A. Walsh, N. C. Greeham, E. A. Marseglia, R. H. Friend, S. C. Moratti, and A. B. Holmes. Efficient photodiodes from interpenetrating polymer networks. *Nature*, 376:498, 1995.
- [7] M. G. Harrison, J. Grüner, and G. C. W. Spencer. Analysis of the photocurrent action spectra of MEH-PPV polymer photodiodes. *Physical Review B*, 55:7831, 1997.
- [8] P. R. Karmel, G. D. Colef, and R. L. Camisa. *Introduction to Electromagnetic and Microwave Engineering*. Wiley-Interscience, December 1997.
- [9] D. Kearns and M. Calvin. Photovoltaic Effect and Photoconductivity in Laminated Organic Systems. *Journal of Chemical Physics*, 29:950, 1958.
- [10] H. A. McCartney and M. H. Unsworth. Spectral distribution of solar radiation. I: direct radiation. *Quarterly Journal of the Royal Meteorological Society*, 104:699, 1978.
- [11] L.A.A. Pettersson, L.S. Roman, and O. Inganäs. Modeling photocurrent action spectra of photovoltaic devices based on organic thin films. *Journal of Applied Physics*, 86:487, 1999.
- [12] M. Pope and C. E. Swenborg. *Electronic Processes in Organic Crystals*. Clarendon Press, February 1982.
- [13] T. Stübinger and W. Brütting. Exciton diffusion and optical interference in organic donor-acceptor photovoltaic cells. *Journal of Applied Physics*, 90:3632, 2001.
- [14] C. W. Tang. Two-layer organic photovoltaic cell. *Applied Physics Letter*, 48:184, 1986.
- [15] C. W. Tang and A. C. Albrecht. Photovoltaic Effects of Metal - Chlorophyll-a - Metal Sandwich Cells. *Journal of Chemical Physics*, 62:2139, 1975.
- [16] Q. Wang. *Foundations of Electromagnetic Theory*. Tsinghua University Press, February 2001.